ANL-ART-233

Deformation Mechanism of Aged Hardened Alloy 709 Materials

Nuclear Science and Engineering Division

ANL-ART-233

Deformation Mechanism of Age Hardened Alloy 709 Materials

Prepared by

Xuan Zhang

Nuclear Science and Engineering Division

Argonne National Laboratory

Ting-Leung Sham

Reactor Systems Design & Analysis Division

Idaho National Laboratory

Meimei Li

Nuclear Science and Engineering Division

Argonne National Laboratory

September 2021

ABSTRACT

This report provides an in-depth study of the microstructures of creep-deformed Alloy 790 materials. Five specimens, all creep-tested at 600°C under 330 MPa to failure, were investigated. The creep specimens were machined from plates fabricated by different melt practices, Argon Oxygen Decarburization (AOD), or AOD followed by Electroslag remelting (ESR), and different heat treatments: 1100 or 1150°C Solution Anneal (SA), and some with additional Precipitation Treatment (PT) of 775°C for 10 hours. TEM samples were made from the gauge and the grip sections of each creep-deformed specimen. Bright-field (BF) imaging, high-angle annular dark field (HAADF) imaging, and energy dispersive x-ray spectroscopy (EDS) using a scanning transmission electron microscope (STEM) were carried out on all the samples.

The study provided quantitative information regarding the subgrain structures and the precipitation on grain boundaries, twin boundaries and grain interiors for both the gauge and the grip regions of the specimens. The correlation between the microstructure and the creep performance were briefly discussed. It is likely that the difference in the precipitate distribution leads to the difference in creep life between the SA and the PT specimens. The conditions under which these specimens were tested were accelerated test conditions, designed for short-term scoping and ranking of different melt practices and heat treatment conditions. The pre-straining of the creep specimens was in the order of 4 to 5% total strain. Future work will focus on creep-deformed Alloy 709 specimens that were tested at more prototypical conditions where the applied stresses were below yield.

ACRONYMS

ANL	Argonne National Laboratory
AOD	Argon oxygen decarburization
ART	Advanced Reactor Technologies
ASME	American Society of Mechanical Engineers
ASTM	ASTM, International (formerly, the American Society for Testing and Materials)
BF	Bright Field
BPVC	Boiler and Pressure Vessel Code
CNM	Center for Nanoscale Materials
CTB	Coherent twin boundary
DOE	Department of Energy
EDS	Energy dispersive X-ray spectroscopy
ESR	Electro-slag remelting
FY	Fiscal year
GB	Grain boundary
HAADF	High-angle annular dark field
HOMO	Homogenized
INL	Idaho National Laboratory
ITB	Incoherent twin boundary
PT	Precipitation treatment
SA	Solution annealing
STEM	Scanning transmission electron microscopy
TB	Twin boundary
TEM	Transmission electron microscopy
US	United States of America

TABLE OF CONTENTS

LIST OF TABLES

LIST OF FIGURES

1 Introduction

Improved structural materials are a key element in the development of advanced nuclear energy systems. Alloy 709 is an advanced austenitic stainless steel containing nominally 20% Cr and 25% Ni that was developed for enhanced creep performance and oxidation resistance, when compared to the conventionally used 316H stainless steel, for emerging applications in the nuclear industry (S. Sham & Natesan, 2017). The fabrication scale-up effort for Alloy 709 culminated in the procurement of the first commercial heat from Electralloy/G. O. Carlson by the US Department of Energy (DOE), totaling about 45,000 lb. The heat number is 58776. Three ingots, processed by Argon-Oxygen-Decarburization (AOD), AOD followed by Electroslag Remelting (ESR), and ESR followed by homogenization (ESR-HOMO) routes, were fabricated. Each ingot was rolled into three plates, and each plate was solution annealed (SA) at 1050, 1100, or 1150°C. The totaling nine materials conditions were denoted as process condition + SA temperature with a "-SA" suffix; for example, the ESR plate that was SA at 1100°C is named ESR1100-SA.

It is believed that the improved high temperature creep strength of Alloy 709 relative to 316H is derived from the precipitation of a high density of fine-scale secondary phases during straining at elevated temperatures. Those precipitates can serve as the pinning sites for dislocation glide, effectively increasing the back stress (threshold stress) of the material, resulting in a reduced effective stress (Sandström, Farooq, & Zurek, 2013; Vujic, Sandström, & Sommitsch, 2015). However, there are concerns that likely precipitates, typically the MX (M=Ti/Nb, X = N/C) or Z-phase in a Nb/Ti-containing and N-stabilized stainless steel such as the Alloy 709, will not be able to form in a timely manner in low temperature conditions due to the slow kinetics (T.-L. Sham, Zhang, & Young, 2019). This leads to the desire to develop a precipitation treatment (PT), aimed at bringing out those precipitates prior to putting the material in service. A 775°C/10h recipe was formulated and the PT materials were characterized in FY19 (T.-L. Sham et al., 2019) and FY20 (X. Zhang & Sham, 2020). The characterization showed that the PT resulted in the formation of ~20 nm sized Nb-rich phase (MX or Z-phase) preferentially on dislocations.

Scoping tests of the ESR1100-SA, ESR1150-SA, ESR1100-PT and ESR1150-PT materials performed at the Idaho National Laboratory (INL) reported that the PT has likely resulted in somewhat shorter creep rupture lives compared to the SA (but still superior to 316H), although this disadvantage diminished at higher temperatures and lower stresses; for example, under 925°C/27MPa condition, limited data shows that the ESR1150-SA and ESR1150-PT have near equivalent creep life (Rupp & McMurtrey, 2020a). On the other hand, the PT significantly increased the number of cycles to failure in strain-controlled fatigue and creep-fatigue tests, with the cyclic peak stresses from the PT specimens lower than those from the SA specimens (Rupp & McMurtrey, 2020a). Due to the multi-fold effects, it was determined that the PT resulted in balanced properties among the different types of mechanical properties, and the ESR1150-PT material was selected to receive further testing for developing the data package needed to qualify Alloy 709 in Section III, Division 5 of the ASME BPVC (Rupp, Wang, Zhang, & Sham, 2021).

The goal of the research presented in this report is to characterize the deformation microstructures of the 600°C/330MPa creep-tested specimens of both SA and PT conditions of ESR1100 and ESR1150 materials (results from an AOD1100-SA specimen is also presented), using the transmission electron microscopy (TEM) techniques. TEM samples were made from the gauge (i.e. contains plastic deformation) and the grip sections of each specimen. The stresses at

the grips are below yield and hence there is no plastic deformation. The study focuses on the similarities and differences of the microstructure between the SA and the PT specimens. Quantitative information regarding the subgrain structures and the precipitation on grain boundaries, twin boundaries and grain interiors is presented. This study is a part of an on-going effort in investigating the deformation microstructures of Alloy 709 under creep, fatigue, and creep-fatigue conditions. Similar study on the fatigue and creep-fatigue specimens will be carried out in future work.

2 Materials and methods

The product chemistry of the AOD and ESR conditions of Alloy 709 heat 58776 is listed in wt.% in Table 2-1. Minimal differences exist between the two melt practices.

Five creep-tested specimens, each from the AOD1100-SA, ESR1100-SA, ESR1150-SA, ESR1100-PT, and ESR1150-PT conditions, are assessed in this study. As noted previously, the "SA" in the condition name indicates that the specimen has been solution annealed at the designated temperature, and the "PT" indicates that the specimen has been treated at 775°C for 10 hours after SA. All the virgin specimens had a 6.35-mm (0.25") gauge diameter and a gauge length of 31.75 mm (1.25"). The specimen length direction is parallel to the rolling direction. All creep tests were performed at 600°C under 330 MPa in air. The details of the creep test for AOD1100-SA are given in (Natesan et al., 2018). The details of the creep test for ESR1100-SA are given by (McMurtrey, 2018), for ESR1100-PT and ESR1150-SA by (McMurtrey & Rupp, 2019), and for ESR1150-PT by (Rupp & McMurtrey, 2020a, 2020b). Table 2-2 summarizes the creep test results. It is seen that the loading strain of those tests were between 3 and 6%, indicating that the load level (330 MPa) was a mechanically aggressive test condition. Figure 2-1 shows the creep curves. It is seen that 1) for the three SA specimens, the AOD1100-SA has the shortest life (1752 h) while the ESR1150-SA has the longest life (3690 h), and 2) PT has significantly improved the total elongation (21.3% → 43.3% for ESR1100 and 30.8% → 45.1% for ESR 1150) but shortened the life (2386 h → 1524 h for ESR1100 and 3690 h → 1387 h for ESR1150). It is noted that data scatter in rupture lives is generally large.

Figure 2-2 shows the photographs of the broken specimens, with the locations of the TEM samples marked. For each specimen, thin slices were cut out from the gauge region with uniform deformation (i.e. outside of the necking area; hereafter named the gauge samples) and from the grip region which had no plastic deformation as the average stress was below yield (hereafter named the grip samples). Those slices were mechanically polished down to ~100 μm in thickness, after which 3 mm discs were punched out. The discs were then electro-jet polished until electron transparent with an electrolyte of 5% perchloric acid and 95% methanol at −40°C under 28 volts with a Struers TenuPol-5 jet polisher. For some of the gauge samples, the existence of cracks or voids from the creep damage led to an early termination of the jet polishing process. For those samples, low energy ion milling using a Fischione TEM mill system at the Center for Nanoscale Materials (CNM) at ANL was performed after the jet polishing to further reduce the thickness.

In addition to making TEM samples from the creep-tested specimens, 3mm-disc TEM samples were also prepared from the as-received AOD1100-SA, ESR1100-SA and ESR1150-SA plate materials, serving as the reference of the creep-deformed microstructures. The as-received ESR1100-PT and ESR1150-PT materials have been previously studied under the TEM (Zhang et al., ANL-ART-192, 2020), and this effort was not duplicated in this work.

The TEM specimens were studied using the FEI Talos F200X TEM/STEM at the CNM. The operating voltage was 200 kV. STEM mode was used; high-angle annular dark field (HAADF) images and bright field (BF) images were collected. Energy dispersive x-ray spectroscopy (EDS) was used to map the chemical composition of selected areas of interest.

Table 2-1. Chemical composition of the AOD and the ESR conditions of Alloy 709 heat # 58776 (in wt.%)

	C	Mn	Si	P	S	Cr	Ni	Mo
AOD	0.07	0.91	0.44	0.014	< 0.000	19.93	24.98	1.51
ESR	0.066	0.90	0.38	0.014	0.001	20.05	25.14	1.51

	N	Nb	Ti	Cu	Co	Al	B	Fe
AOD	0.148	0.26	0.04	0.06	0.02	0.02	0.0045	Bal.
ESR	0.152	0.26	0.01	0.06	0.02	0.02	0.0030	Bal.

Bal. = Balance

Table 2-2. Creep data for the five specimens studied in this report (McMurtrey, 2018; McMurtrey & Rupp, 2019; Natesan et al., 2018; Rupp & McMurtrey, 2020a, 2020b). Test condition was 600°C, 330 MPa.

Material	Specimen ID	Test lab	Creep life (h)	Minimum creep rate (%/h)	Elongation (%)	Area reduction (%)	Loading strain (%)
AOD1100-SA	4B2-2	ANL	1752	3.68E-03	26.0	34.4	~ 6
ESR1100-SA	E-BB1-C1	INL	2386	2.20E-03	21.3	33.9	4.87
ESR1150-SA	E-BC1-C3	INL	3690	1.60E-03	30.8	39.8	5.60
ESR1100-PT	D-775-C1	INL	1524	5.11E-03	43.3	55.0	4.29
ESR1150-PT	BCHT-IC-1	INL	1387	7.22E-03	45.1	51.5	3.87

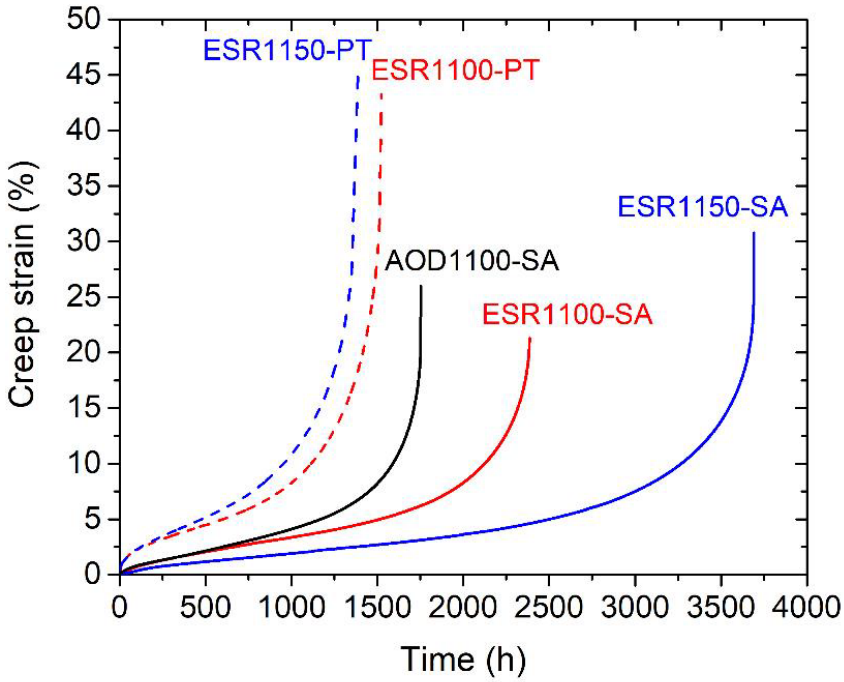

Figure 2-1. Creep curves of the five specimens studied in this report. Test condition was 600°C, 330 MPa. Data was reproduced from references (McMurtrey, 2018; McMurtrey & Rupp, 2019; Natesan et al., 2018; Rupp & McMurtrey, 2020a, 2020b).

Figure 2-2. Photographs of the AOD1100-SA, ESR1100-SA, ESR1150-SA, ESR1100-PT and ESR1150-PT crept specimens. The yellow markers indicate the locations that the TEM specimens were prepared from. The photograph of the AOD1100-SA specimen has been reported previously (Natesan et al., 2018).

3 Microstructure of as-received materials

Figure 3-1 shows the microstructures of the as-received AOD1100-SA, ESR1100-SA, and ESR1150-SA materials, in lower (5,000×, top row) and higher magnifications (14,000×, bottom row). It is observed that the 1100°C SA did not fully recover the deformation induced by rolling, represented by a high density of dislocations in the slip direction, while the 1150°C SA dramatically reduced the dislocation density. The dislocation densities were about 3×10^{13}, 1×10^{13}, and 2×10^{12} m^{-2}, for AOD1100-SA, ESR1100-SA, and ESR1150-SA, respectively. In addition, compared to ESR1100-SA, ESR1150-SA has a much lower density for the residual MX particles (hereafter referred to as the primary MX). The average particle sizes, assuming the particles are spherical, are 129, 86, and 111 nm for AOD1100-SA, ESR1100-SA, and ESR1150-SA, respectively. Assuming a film thickness of 100 nm, the particle densities are 0.66×10^{19}, 4.21×10^{19}, and 0.58×10^{19} m^{-3} for AOD1100-SA, ESR1100-SA, and ESR1150-SA, respectively. As the primary MX is actually (Nb,Ti)N (see Figure 3-2), this means that more Nb, Ti, and N atoms are in solution for ESR1150-SA than ESR1100-SA. For all the materials, the grain boundaries (GBs) and the twin boundaries (TBs) are free of secondary phases.

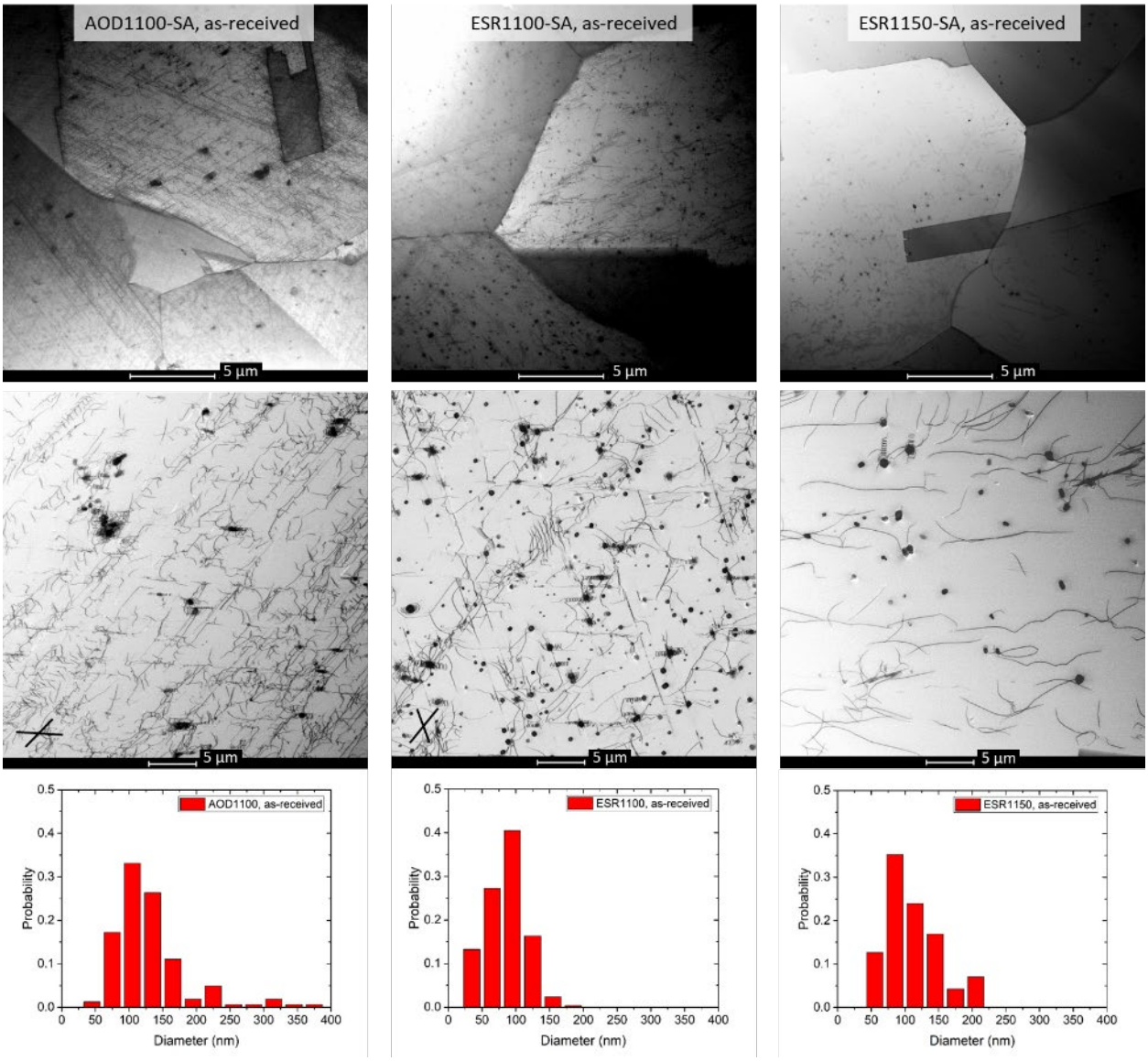

Figure 3-1. BF images showing the microstructures of the as-received AOD1100-SA, ESR1100-SA, and ESR1150-SA materials, in lower (5,000×, top row) and higher magnifications (14,000×, middle row). The particles in the materials are residual MX particles (primary MX) from manufacturing (see Figure 3-2). {111} slip traces are marked on the bottom left corners of the high magnification images of AOD1100-SA and ESR1100-SA. The MX particle size distributions are shown in the bottom row, obtained from 2 to 4 images for each sample.

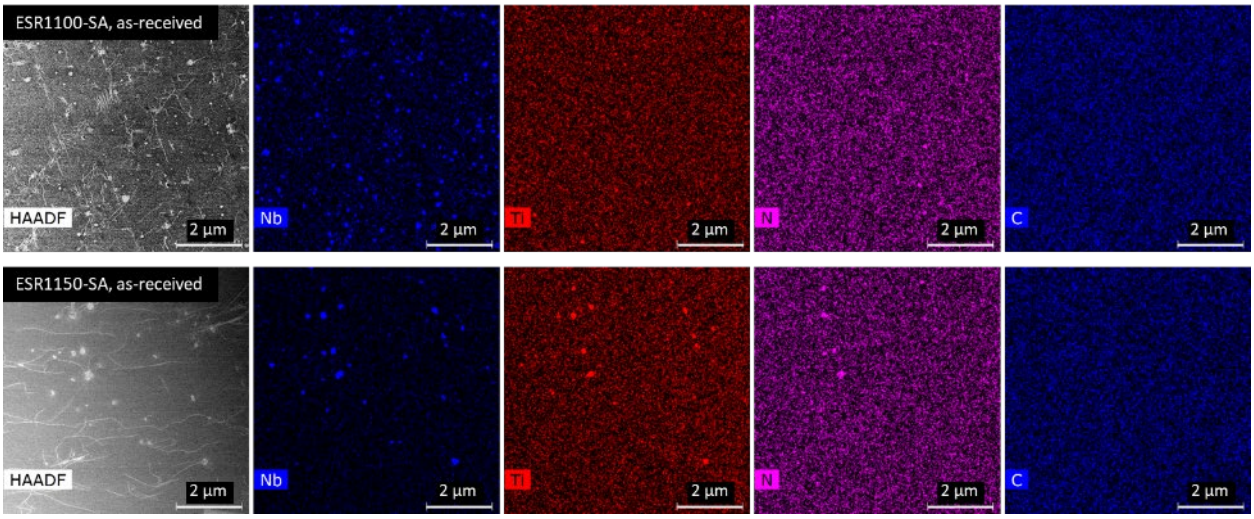

Figure 3-2. EDS maps of the ESR1100-SA and ESR1150-SA imaging areas in Figure 3-1.

The microstructures of the as-received ESR1100-PT and ESR1150-PT have been previously reported (Zhang et al., ANL-ART-170, 2019; Zhang et al., ANL-ART-192, 2020). For an easy access of information, the key observations are repeated here. Figure 3-3 is a combination of two figures from the previous reports. The precipitate types are very similar between the two materials: 1) Nb-rich precipitates of about 20 nm in size, which could be Z-phase or MX phase (further investigation required) and are different from the primary MX particles, have precipitated mainly on the dislocations, the overall density being much lower in ESR1150-PT compared to that in ESR1100-PT due to the lower dislocation density in ESR1150-PT; 2) $M_{23}C_6$ precipitates are decorating the GBs and the incoherent twin boundaries (ITBs), while the coherent twin boundaries (CTBs) are free of precipitates; 3) primary-MX-core/$M_{23}C_6$-shell structured precipitates are found within the grains; 4) µm-long $M_{23}C_6$ chains grow out of the core/shell structured precipitates.

There is, however, one distinct difference between the as-received ESR1100-PT and the ESR1150-PT materials. At high magnifications, Figure 3-4 shows that the matrix of ESR1150-PT contains a high-density of 1-5 nm sized precipitates that are bright in HAADF images, indicating they are enriched in heavier elements such as Nb; in contrast, the matrix of ESR1100-PT is uniform. A possible explanation considers that 1) the as-received ESR1150-SA has more Nb, Ti, and N in solution than ESR1100-SA does due to more primary MX particles being dissolved (refer to Figure 3-1 and the corresponding description), and 2) fewer nucleation sites (dislocations) to precipitate the 20 nm Nb-rich precipitates in ESR1150-PT. As a result, the matrix of ESR1150-PT is more enriched in Nb, Ti and N, thus the aging treatment promoted a more pronounced uniform precipitation of MX or Z-phase in the matrix of ESR1150-PT than that in the matrix of ESR1100-PT.

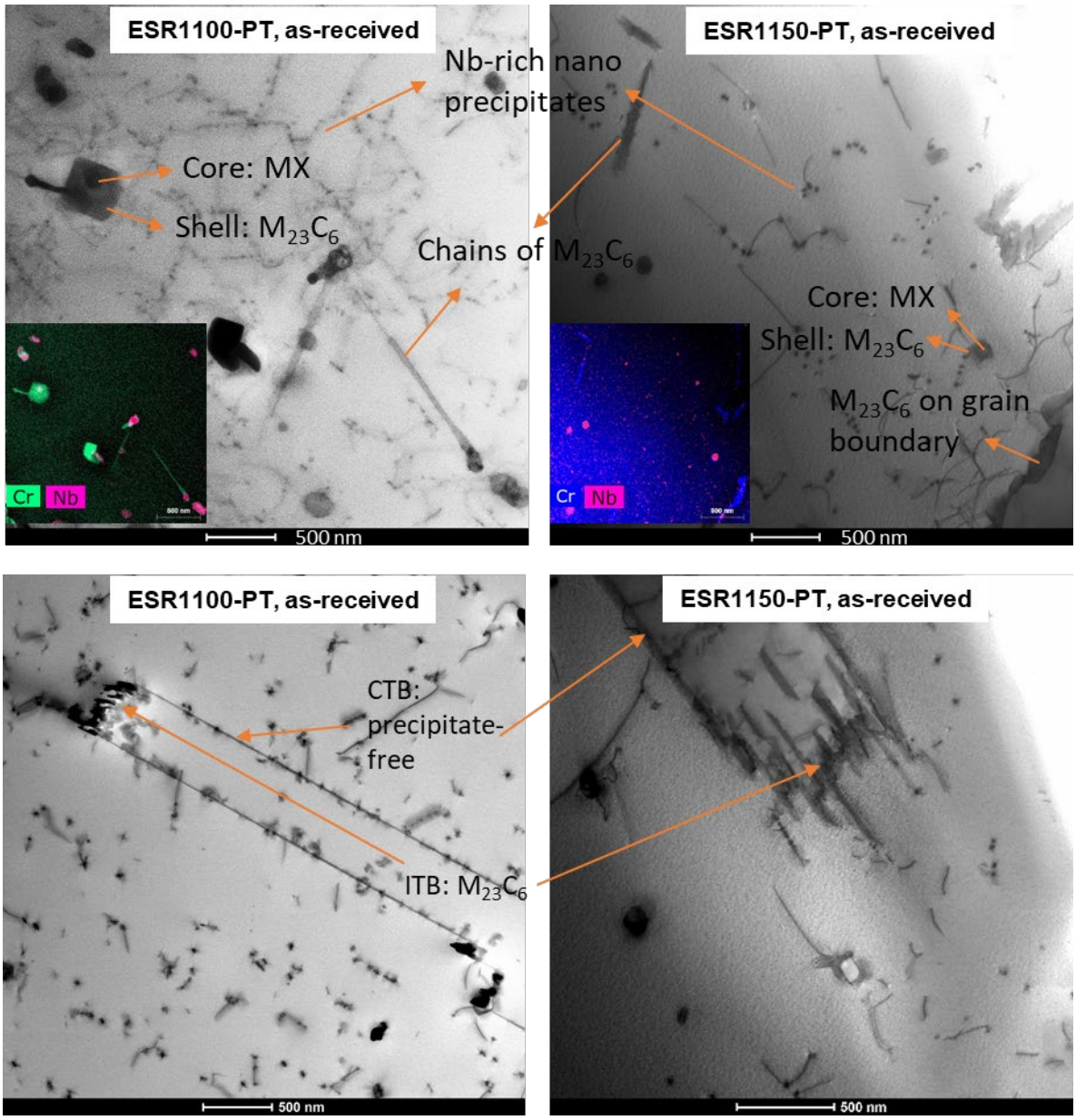

Figure 3-3. BF images of the as-received ESR1100-PT and the ESR1150-PT. Top row shows the grain interiors and a GB in ESR1150-PT, while the bottom row shows the TBs. In all the images, the 20nm-sized Nb-rich precipitates are visible on dislocations.

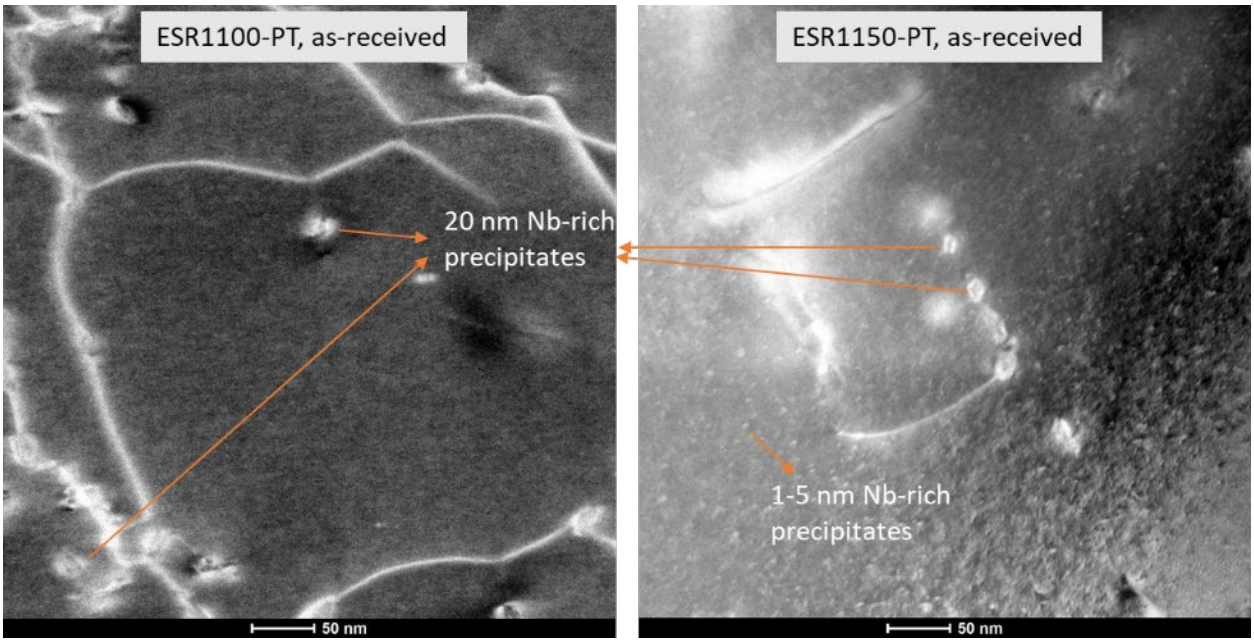

Figure 3-4. HAADF images of the as-received ESR1100-PT and the ESR1150-PT, highlighting the difference in the matrix.

4 Microstructures of creep-tested specimens

This section describes the microstructural observations in the grip and the gauge regions of the 600°C/330MPa creep-tested AOD1100-SA, ESR1100-SA, ESR1150-SA, ESR1100-PT and ESR1150-PT specimens.

4.1 Microstructures of gauge samples

4.1.1 Subgrain and dislocation structures in gauge samples

Figures 4-1 and 4-2 show the microstructures of the gauge samples from the five creep-tested specimens at low (5kx) and intermediate (14kx) magnifications. The creep deformation leads to the formation of subgrain structures, manifested by the global presence of dark and bright areas within the grains due to the variation of crystal orientations. Figure 4-3 shows a closer view of the substructures; it is seen that dislocation cells on the order of 500 nm are visible in some of the grains in all the samples. Figure 4-4 shows the magnified view of the yellow boxed area in the ESR1150-SA sample in Figure 4-3. It is seen that the cell boundary contains a pile of well-organized dislocations. Sometimes the cell boundary dislocations are observed to be pinned by precipitates; an example is shown in Figure 4-5.

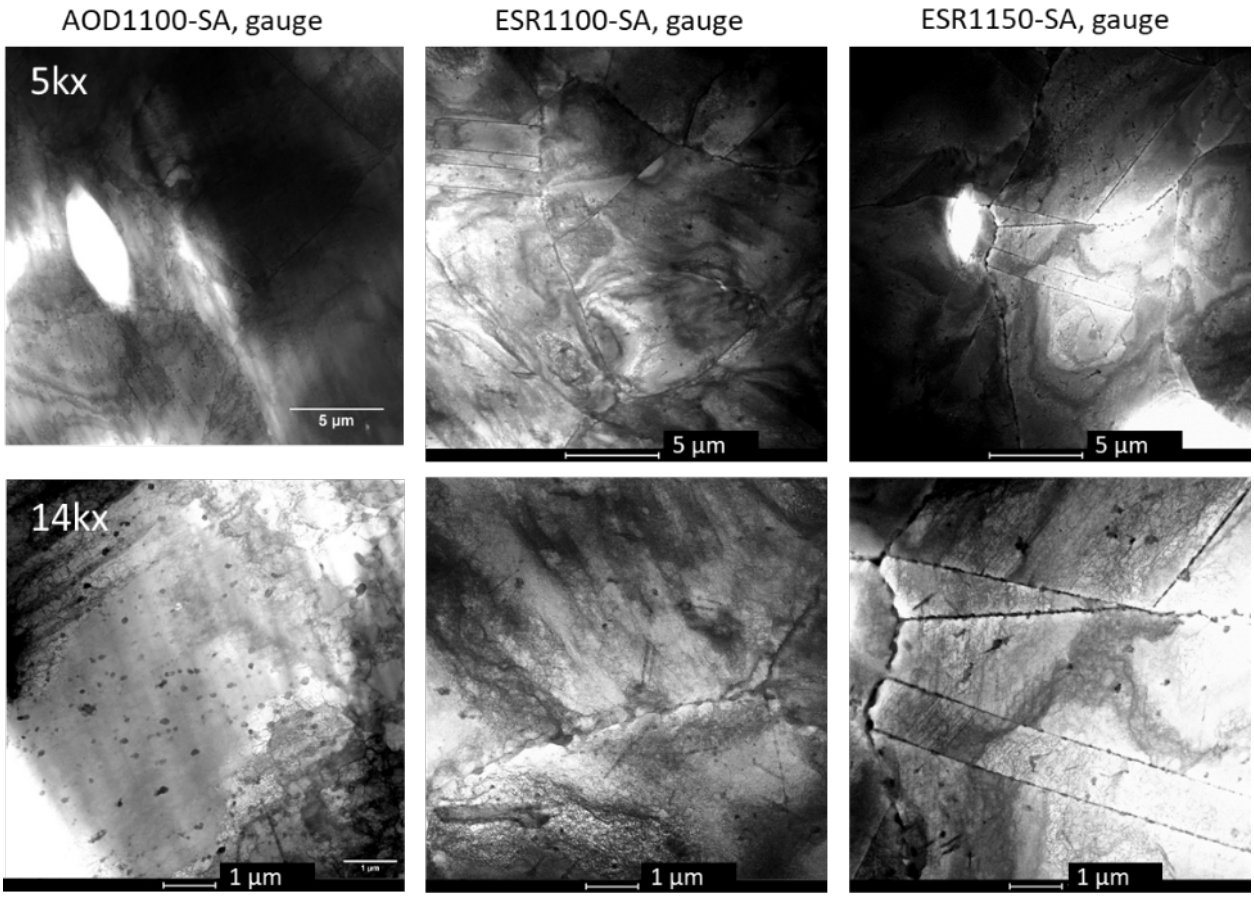

Figure 4-1. BF images showing the microstructures of the gauge samples from the three creep-tested SA specimens at low (5kx) and intermediate (14kx) magnifications.

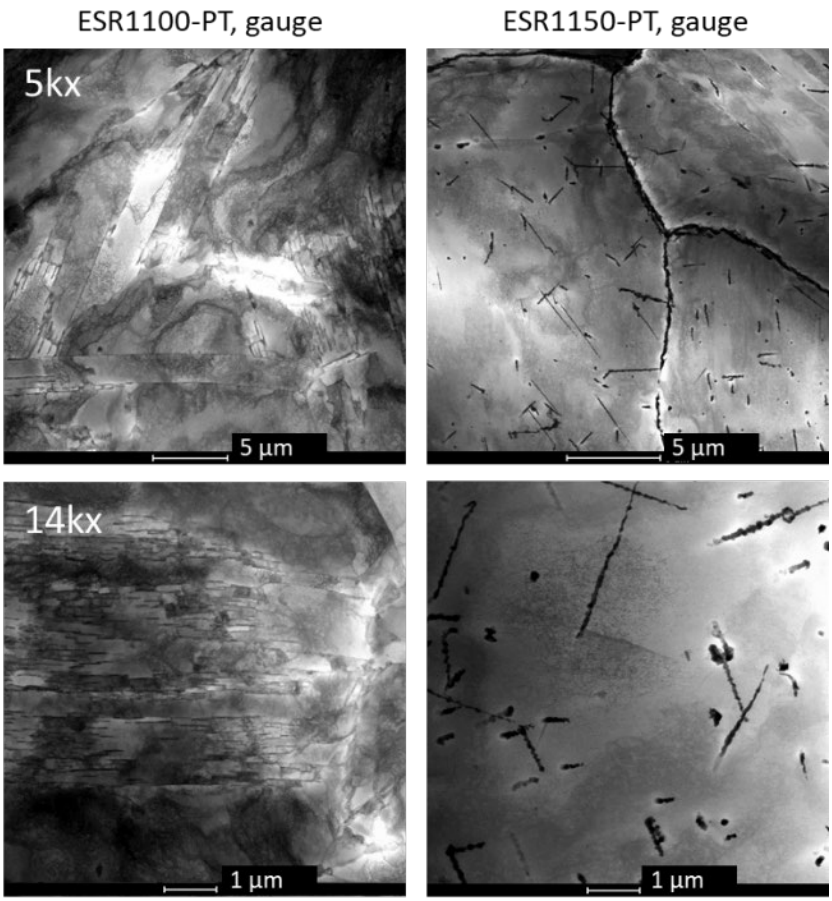

Figure 4-2. BF images showing the microstructures of the gauge samples from the two creep-tested PT specimens at low (5kx) and intermediate (14kx) magnifications.

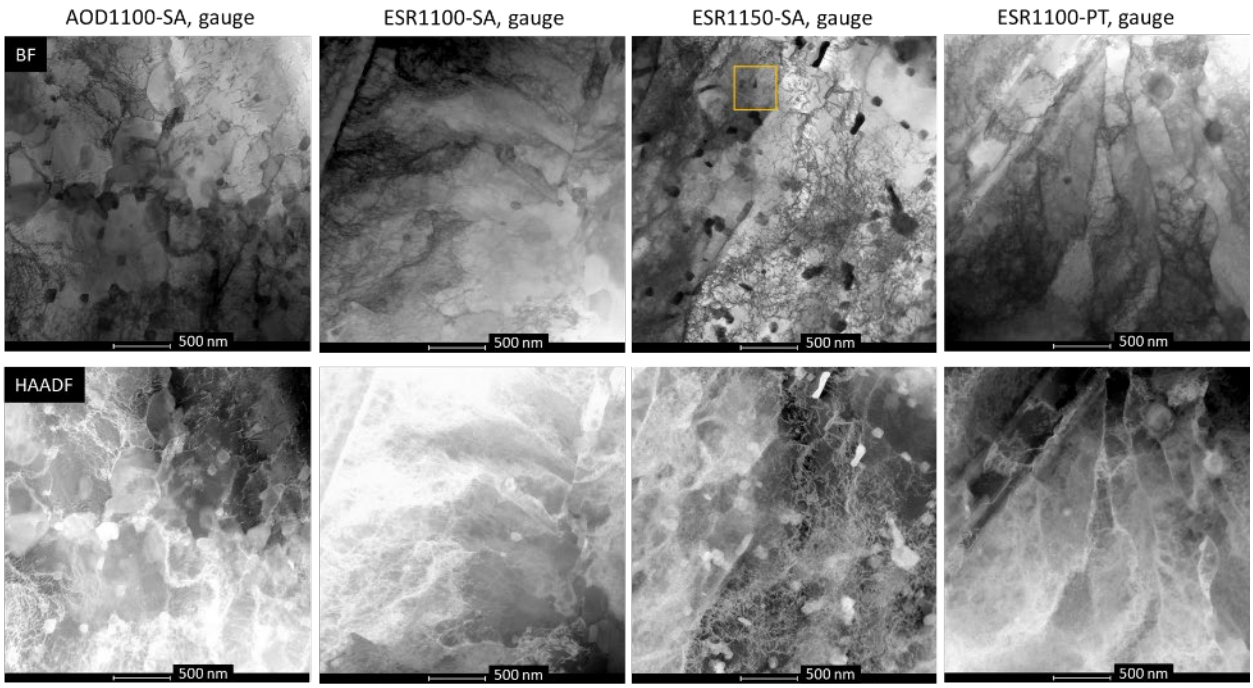

Figure 4-3. BF and HAADF images showing the dislocation cells in four gauge samples.

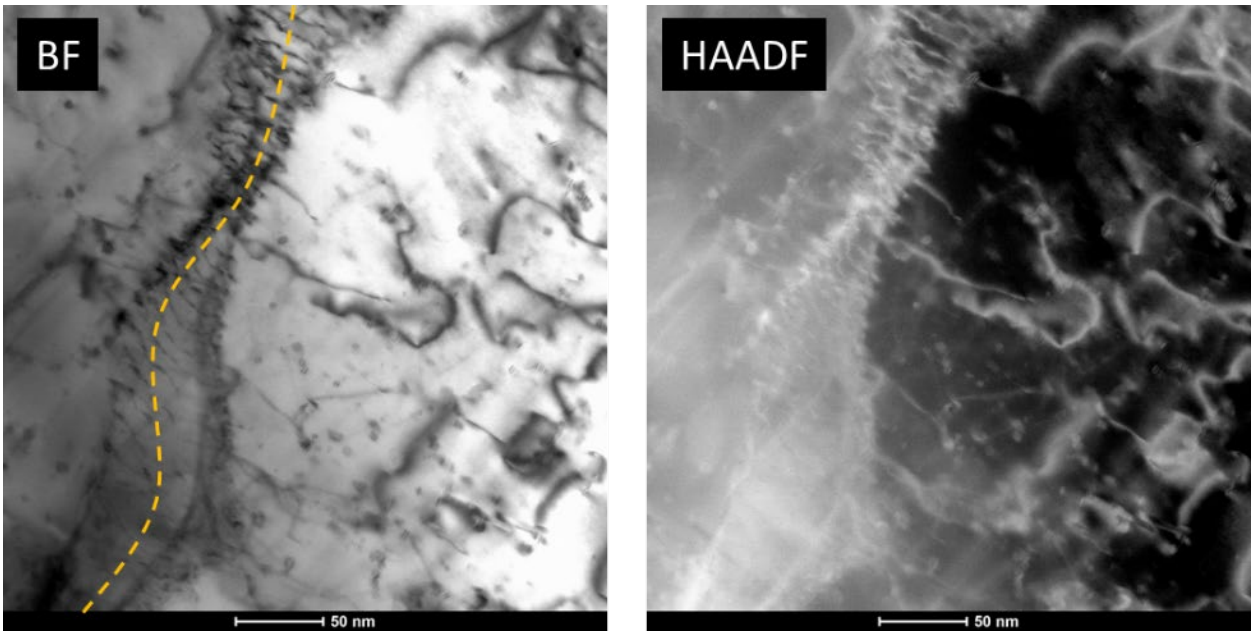

Figure 4-4. A close view of a cell boundary in ESR1150-SA gauge sample. The yellow dotted line marks the boundary.

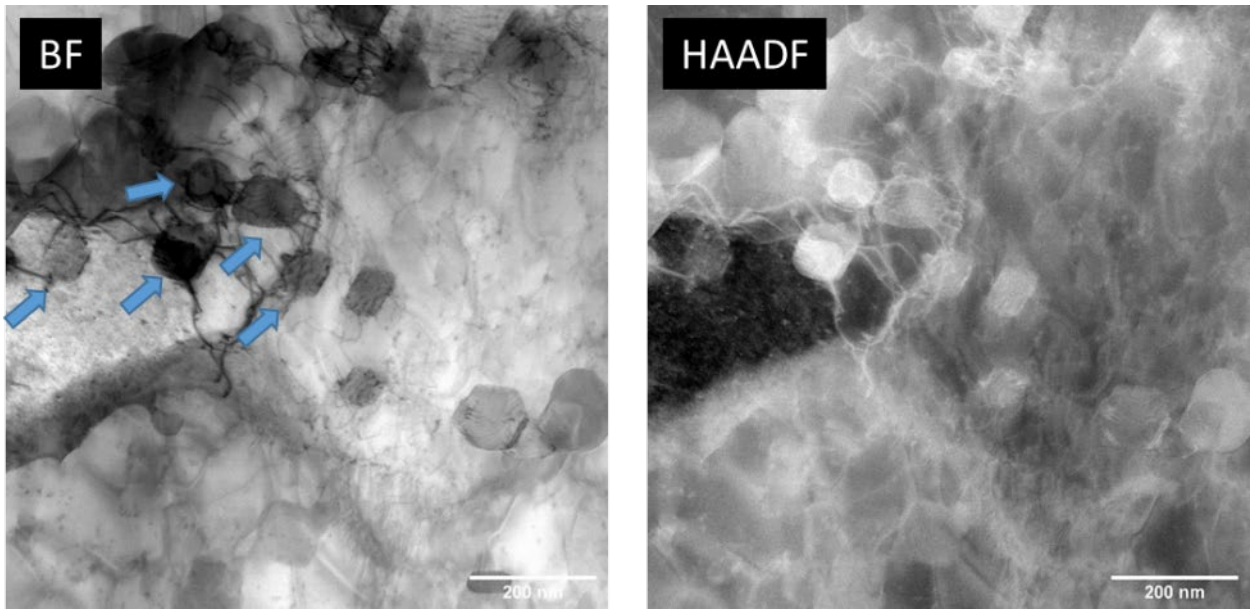

Figure 4-5. A close view of a cell boundary containing precipitates in AOD1100-SA gauge sample. Arrows point to those boundary precipitates.

4.1.2 Precipitates in gauge samples

For the SA specimens, the precipitation happens during deformation, while for the PT specimens, precipitates already exist prior to deformation (Figure 3-3). The precipitates play a vital role in the creep resistance of Alloy 709. The study of the gauge samples reveals a major difference between the deformation microstructures in SA and PT samples, being that in the SA samples, the grain interior contains a high density of $M_{23}C_6$ and $(Cr,Mo)_3Ni_2Si(C,N)$ η phases, while in the PT samples, the grain interior is mostly free of those two phases except some very long (μm-sized) precipitates of low density. Such a difference is clearly shown in Figures 4-6 and 4-7 for the comparison between the ESR1100 SA and PT samples and between the ESR1150 SA and PT samples, respectively.

Figure 4-8 are closer looks of the $M_{23}C_6$ and $(Cr,Mo)_3Ni_2Si(C,N)$ η phases at a GB (top row), a CTB (top row), an ITB (middle row), and grain interiors (bottom row) of ESR1150-SA gauge sample. Those images show that the η phase nucleated on $M_{23}C_6$ carbides. The η phase has been observed co-existing with $M_{23}C_6$ carbides in the 20Cr25Ni-based steels with high nitrogen such as NF709 (Sourmail & Bhadeshia, 2005) and Alloy 709 (Ding et al., 2019; Li, Chen, Zhang, & Natesan, 2018) after extended aging at higher temperatures (650°C and above).

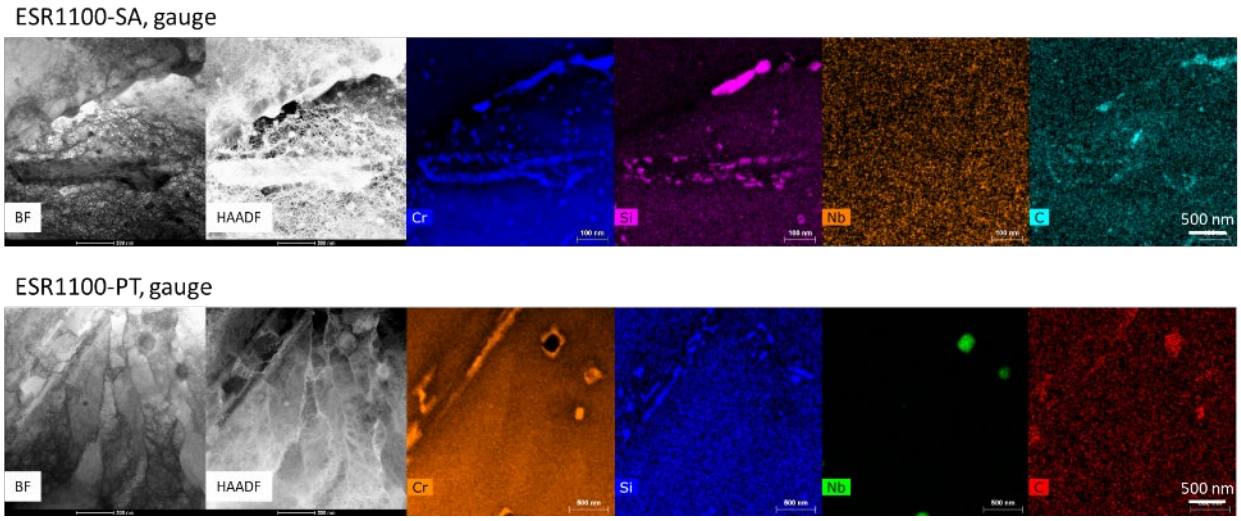

Figure 4-6. Comparison of precipitates between the ESR1100-SA and ESR1100-PT gauge samples.

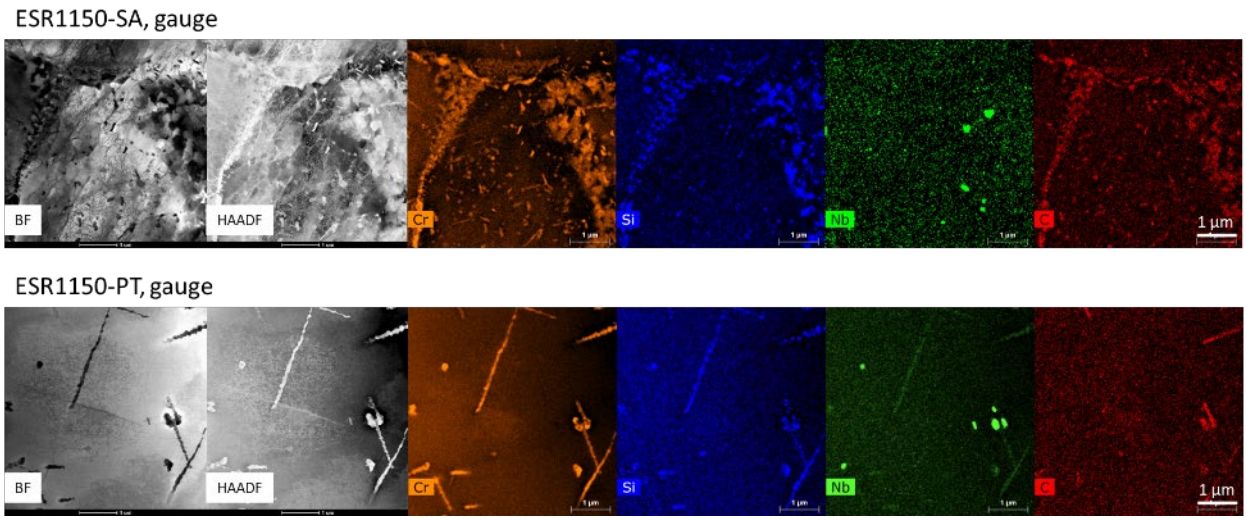

Figure 4-7. Comparison of precipitates between the ESR1150-SA and ESR1150-PT gauge samples.

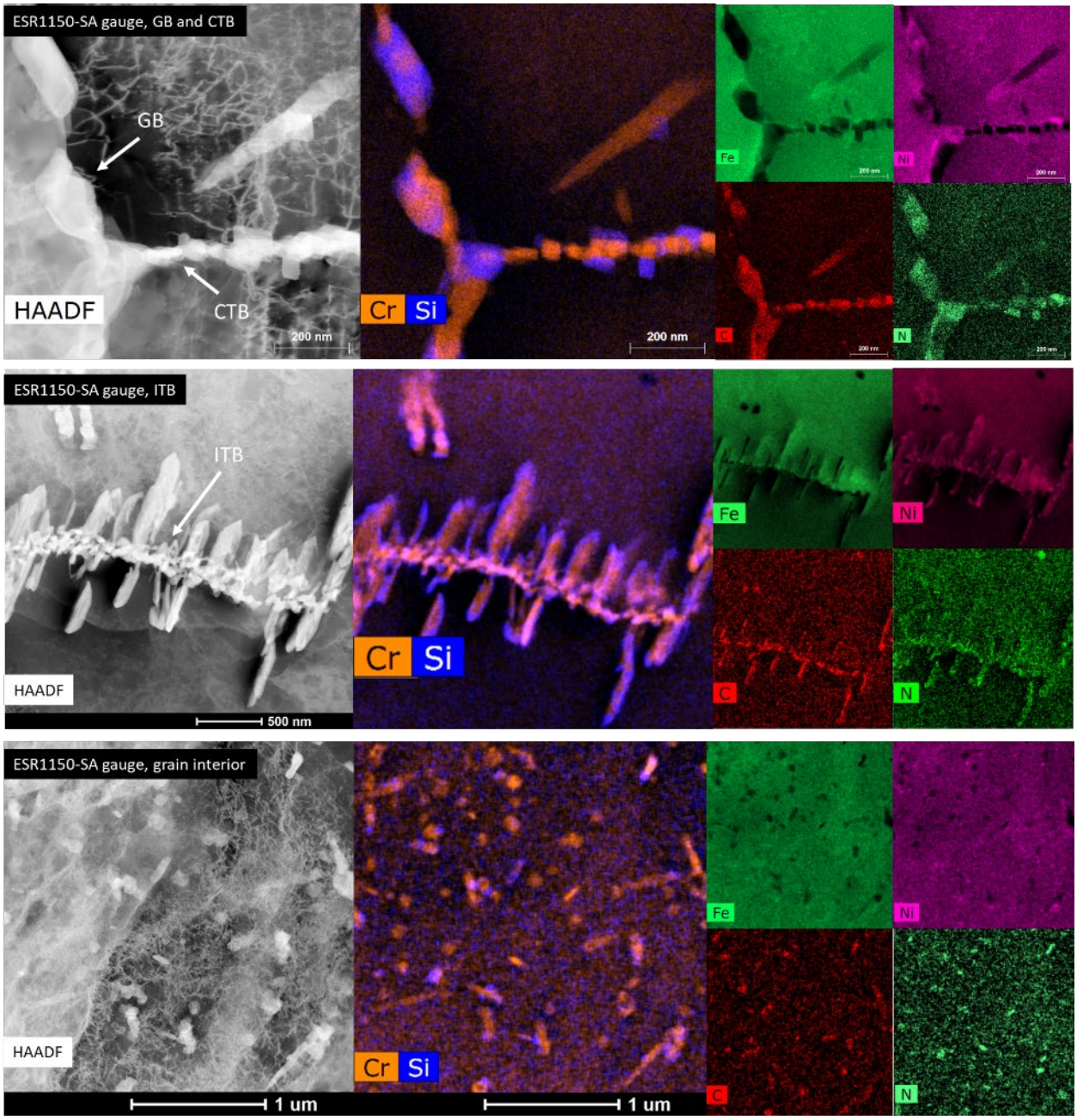

Figure 4-8. HAADF images and EDS elemental maps from the GB (top row), CTB (top row), ITB (middle row), and grain interior (bottom row) of ESR1150-SA showing the co-existing $M_{23}C_6$ and $(Cr,Mo)_3Ni_2Si(C,N)$ η phases.

In PT gauge samples, the co-existing $M_{23}C_6$ and $(Cr,Mo)_3Ni_2Si(C,N)$ η phases are also frequently observed, as shown in Figure 4-9. The local gathering of some plate-like extended precipitates in ESR1100-PT, as shown in Figure 4-9 top row, is associated with the presence of TBs, with their extension direction being parallel to the CTBs.

Figure 4-9 bottom row shows another type of large precipitates that commonly exist in the PT gauge samples, being µm-sized chains of $M_{23}C_6$ carbides decorated with $(Cr,Mo)_3Ni_2Si(C,N)$ η phase particles; the Cr-Si composite map as the inset in Figure 4-9 bottom row shows it better. Those precipitates are likely the $M_{23}C_6$ chains that formed during the PT process (Figure 3-3) that grew longer during the creep test and also had the η phase precipitated on.

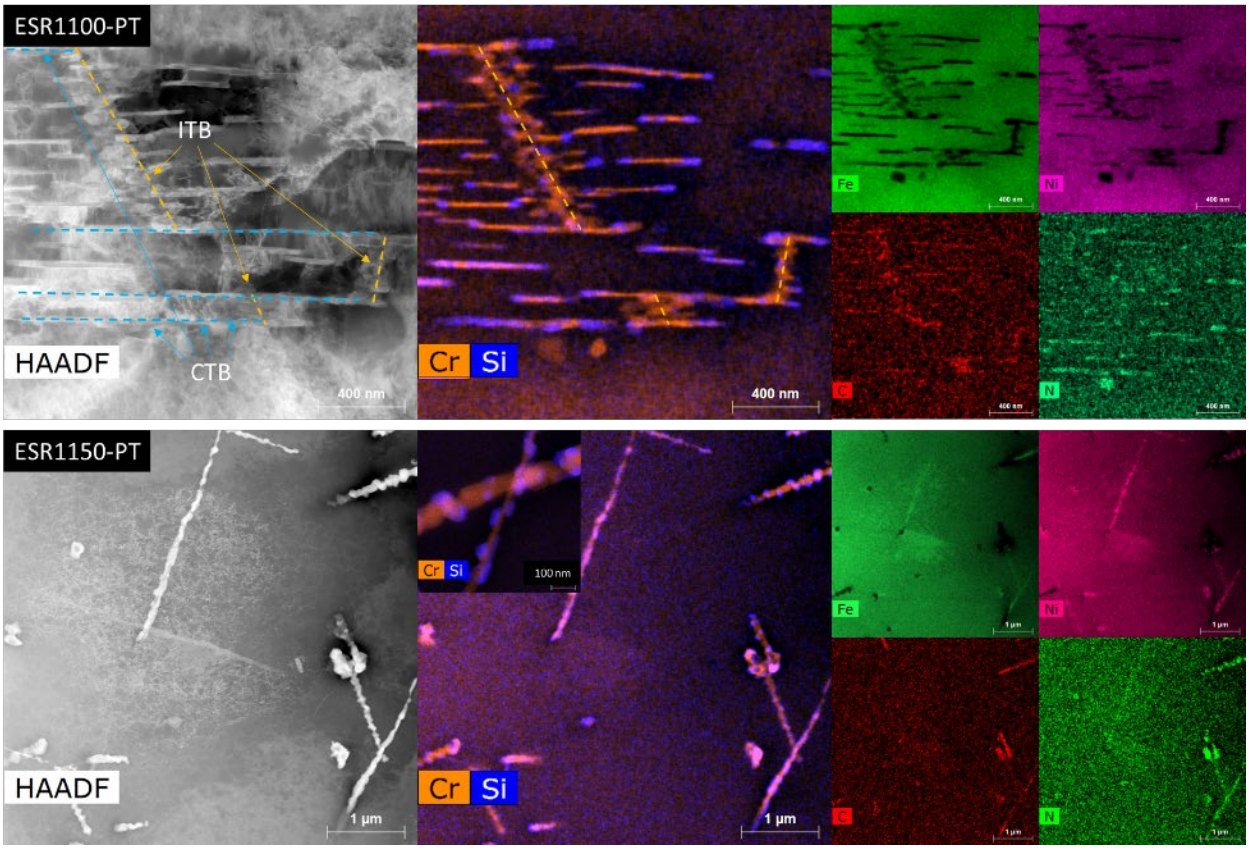

Figure 4-9. HAADF images and EDS elemental maps showing the extended $M_{23}C_6$ carbides and $(Cr,Mo)_3Ni_2Si(C,N)$ η phases in PT gauge samples.

Finally, at very high magnifications, it is observed that common to all the gauge samples, 1-10 nm sized precipitates enriched in Nb are associated with dislocations; see Figure 4-10. Those precipitates could be the MX phase or Z-phase, the determination of which requires further investigation. (Porter et al., 2021) found experimental evidences of nano-sized Z-phase in creep-fatigue tested Alloy 709 material. Those figures confirmed the role of the nano precipitates in pining the dislocation motion during creep, which is a major goal in the alloy design. It is noted that no substantial difference, in terms of the size and density of the nano precipitate, exists between the SA and the PT samples. It is interesting to see that although the PT samples already have some 20-nm sized Nb-rich precipitates precipitated on dislocations prior to the creep test (Figure 3-3), the creep deformation seems to have eliminated the majority of them.

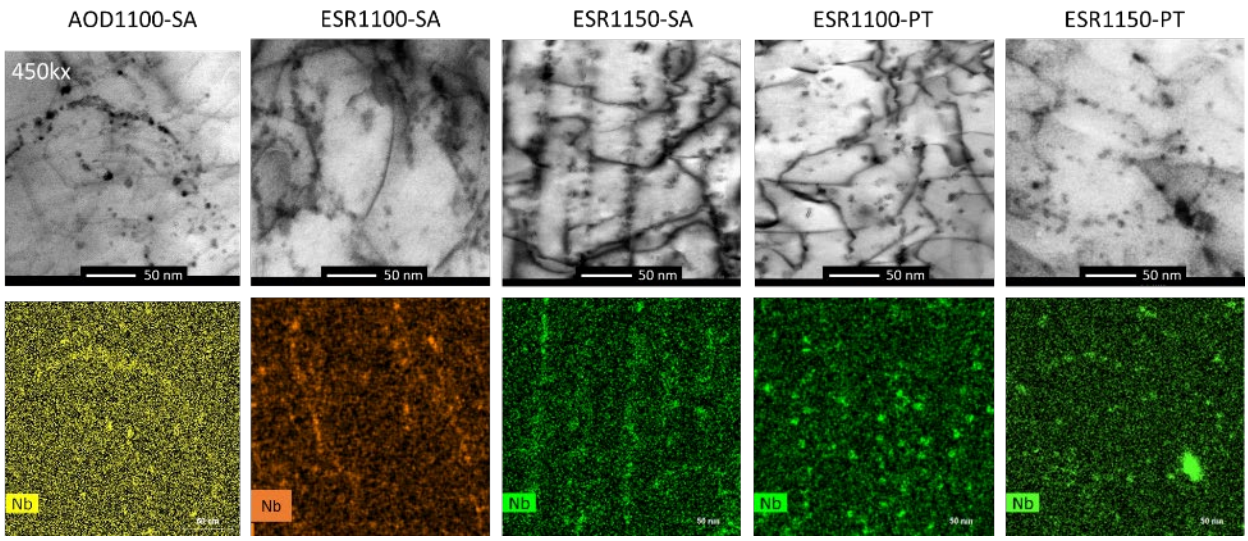

Figure 4-10. BF images and Nb maps showing the 1-10 nm precipitates on dislocations in all the gauge samples.

4.2 Microstructures of grip samples

The grip sections of the creep-tested specimens experienced no plastic deformation and were effectively aged during the course of the 1-hour soaking and the subsequent loading at 600°C, hence the aging time for the grip samples are 1753, 2387, 3691, 1525, and 1388 hours, for AOD1100-SA, ESR1100-SA, ESR1150-SA, ESR1100-PT, and ESR1150-PT grip samples, respectively (refer to Table 2-2 and adding 1 hour to the creep life). For the PT samples, that means the material has experience the 775°C/10 h heat treatment followed by the additional aging at 600°C.

Figure 4-11 shows the microstructures of the grip samples at a low magnification (5kx). There are some common features to all the samples: 1) the grains are well-annealed, equiaxed; 2) the GBs are decorated with the co-existing $M_{23}C_6$ and $(Cr,Mo)_3Ni_2Si(C,N)$ η phases (Figure 4-12); 3) the CTBs are free of precipitates while the ICBs are decorated with the co-existing $M_{23}C_6$ and $(Cr,Mo)_3Ni_2Si(C,N)$ η phases (Figure 4-13 and Figure 4-14); 4) the grain interiors have $M_{23}C_6$ precipitates often formed around primary MX particles, which sometimes evolve into long chains of $M_{23}C_6$ precipitates that almost look like needles (Figure 4-12 and Figure 4-14).

There are also differences between the SA and the PT grip samples. Figure 4-13 shows that the ITBs in the SA samples are less heavily precipitated compared to those in the PT samples, mainly due to the fact that PT itself has already introduced precipitations on ITBs (Figure 3-3) and further aging promoted them to grow.

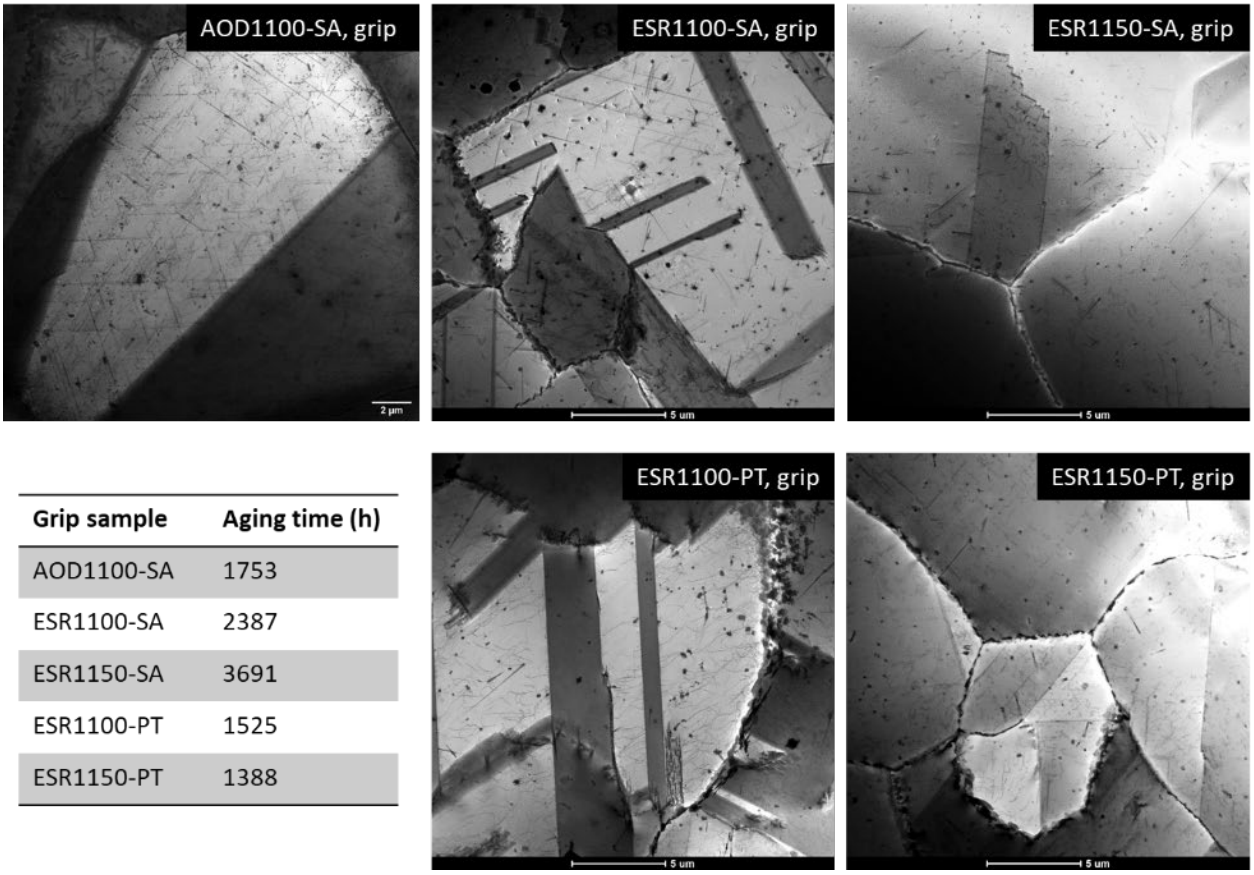

Grip sample	Aging time (h)
AOD1100-SA	1753
ESR1100-SA	2387
ESR1150-SA	3691
ESR1100-PT	1525
ESR1150-PT	1388

Figure 4-11. Low magnification (5kx) BF images showing the microstructures of the grip samples. The effective aging hours at 600°C are listed in the table.

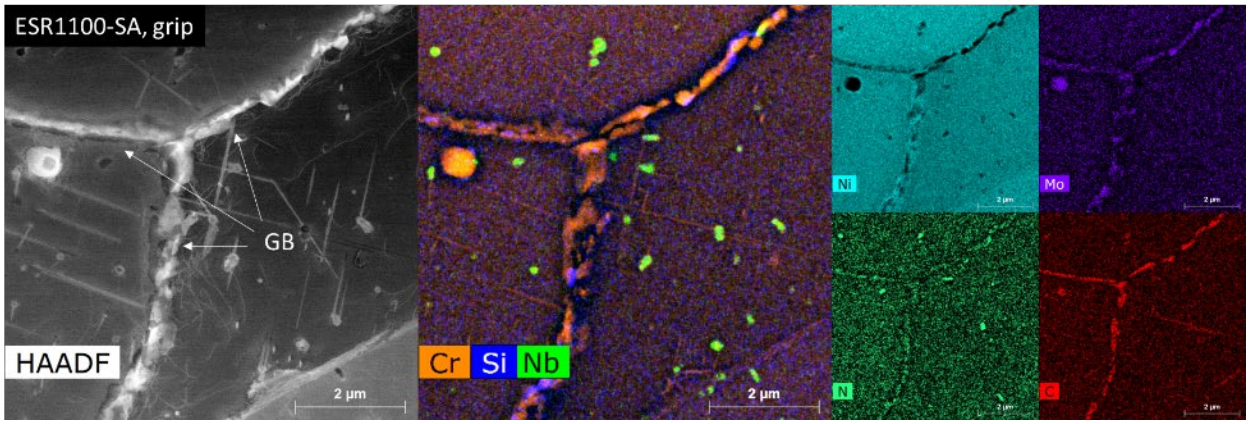

Figure 4-12. An example from the ESR1100-SA grip sample showing the elemental maps for the precipitates at the GBs and within the grain interiors.

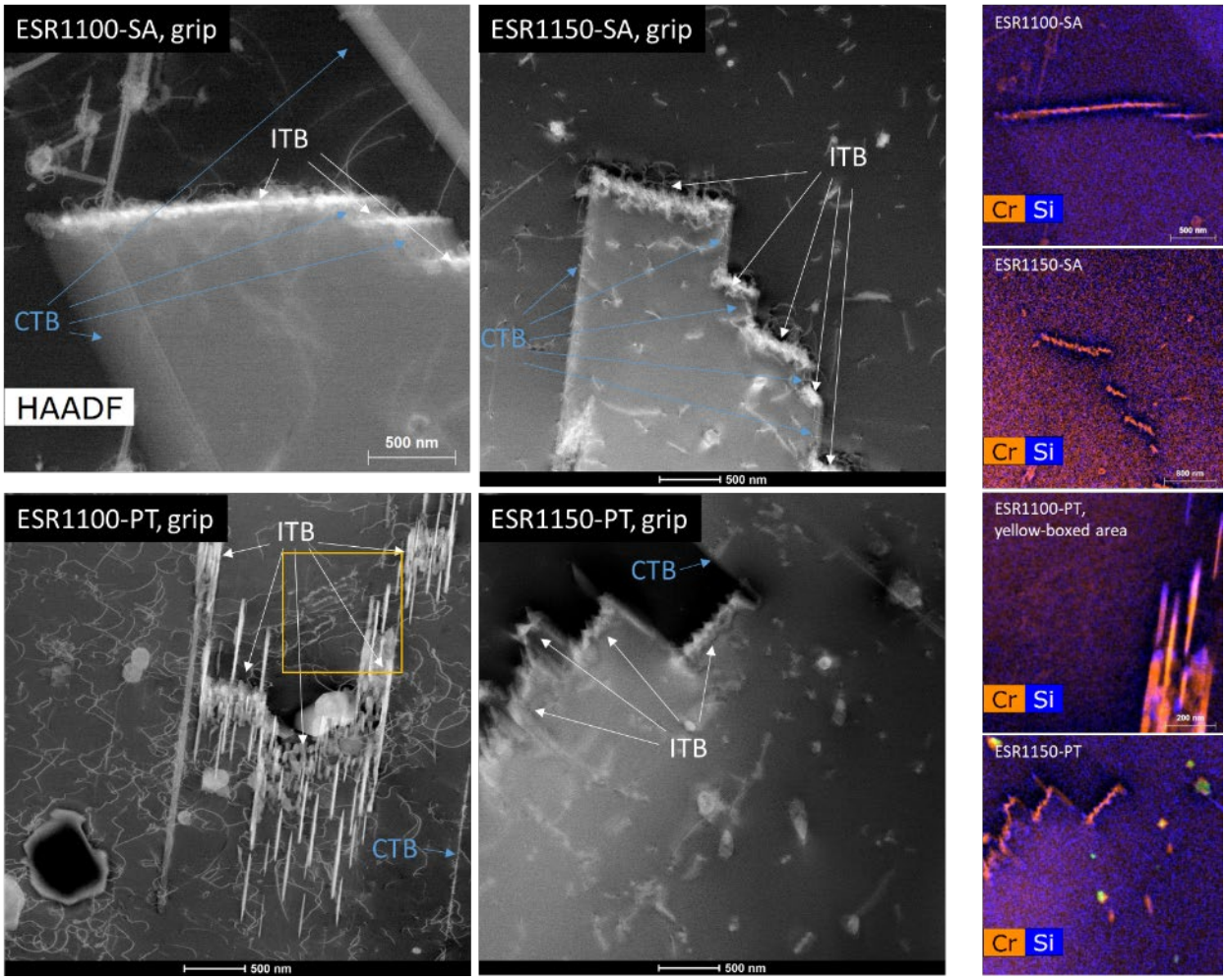

Figure 4-13. HAADF images and the corresponding Cr-Si composite maps of ESR1100-SA, ESR1150-SA, ESR1100-PT and ESR1150-PT grip samples featuring the CTBs and ITBs. Note the difference in the scale bar of the ESR1100-SA image compared to the others.

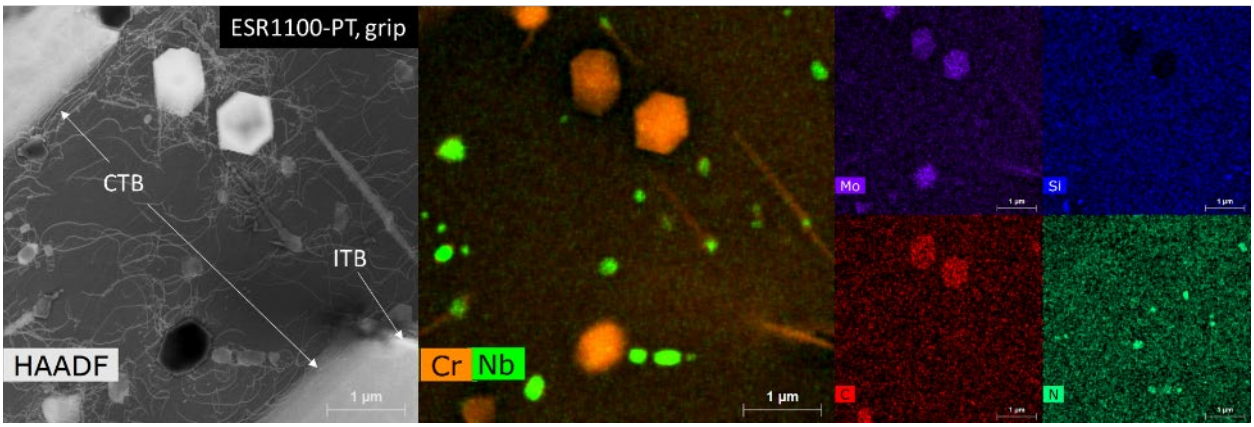

Figure 4-14. An example from the ESR1100-PT grip sample showing the elemental maps for the precipitates at the TBs and within the grain interiors. While all the three largest precipitates are $M_{23}C_6$, the fact that two appear bright and one appears dark in the HAADF images is due to the

relative position of the precipitate with respect to the sample foil: the bright ones are on the top of the foil, while the dark one is buried inside the foil. The carbon map tells the same story.

Another major difference between the SA and the PT grip samples is revealed at higher magnifications, shown in Figures 4-15 and 4-16. In the AOD1100-SA sample, 50-100nm sized $M_{23}C_6$ cuboidal precipitates are observed on dislocations. The closer to the GBs, the more precipitates are observed on dislocations, indicating a flux of Cr and C towards the GB (for more about this point, see (Xuan Zhang, Chen, & Caputo, 2021)). In the ESR1100-SA and ESR1150-SA samples, most of the dislocations are precipitate-free, but very occasionally, 50-100nm sized $M_{23}C_6$ cuboidal precipitates are observed. On the other hand, in the ESR1100-PT and the ESR1150-PT samples, ~20nm-sized precipitates enriched in Nb, Cr and Mo are found on dislocations. The composition suggests that they are the Z-phase ((Cr,Mo)NbN). Compared to the as-received PT samples (Figure 3-3), which already have 20 nm-sized Nb-rich precipitates, it suggests that the additional aging at 600°C for ~1000 hours does not lead to the coarsening of this phase.

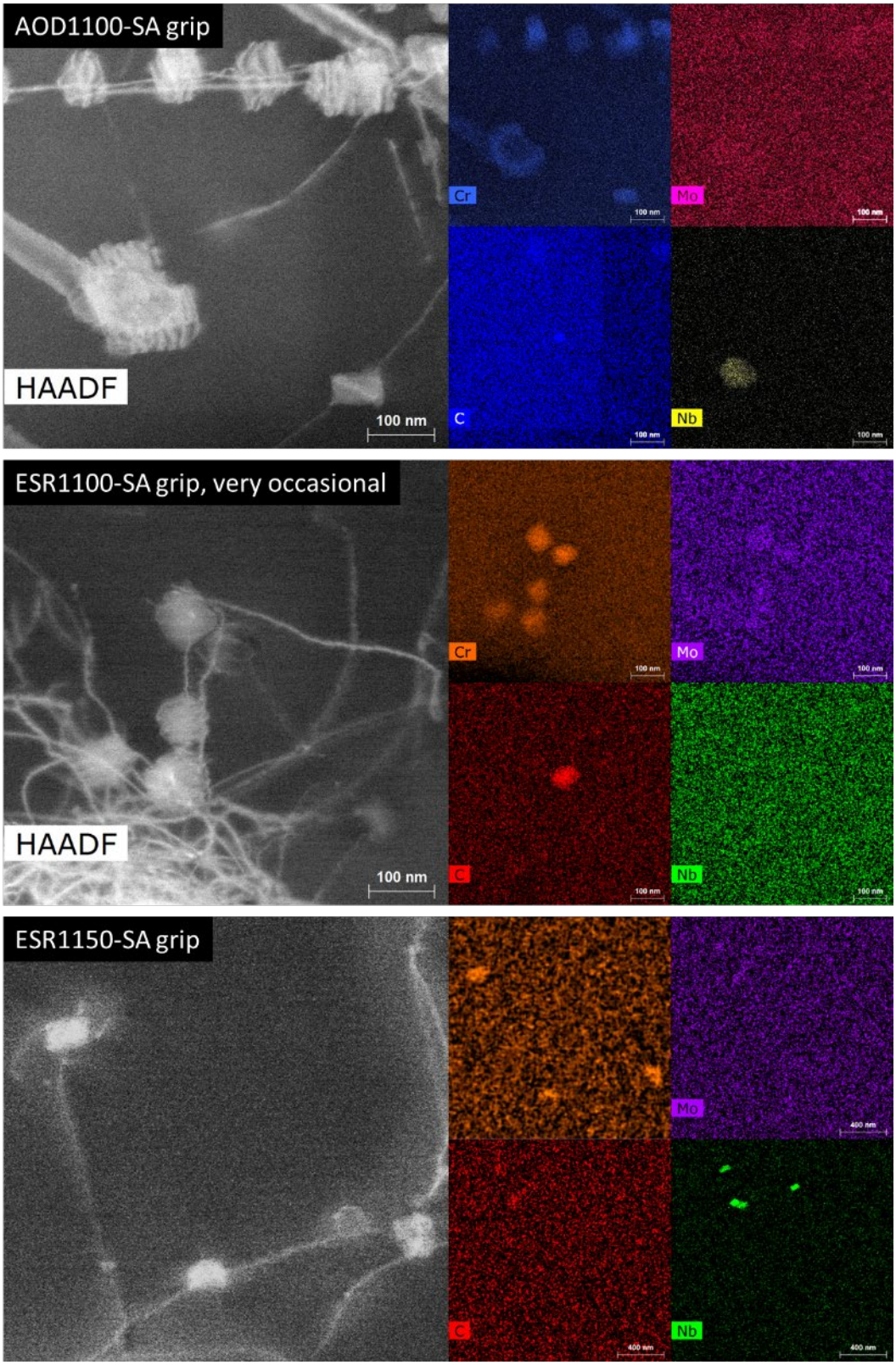

Figure 4-15. HAADF images and EDS elemental maps featuring the $M_{23}C_6$ precipitates on dislocations in the SA samples. The ESR1150 image also has several $M_{23}C_6$ chains included. Note the difference in the magnification of the ESR1100 image compared to the others.

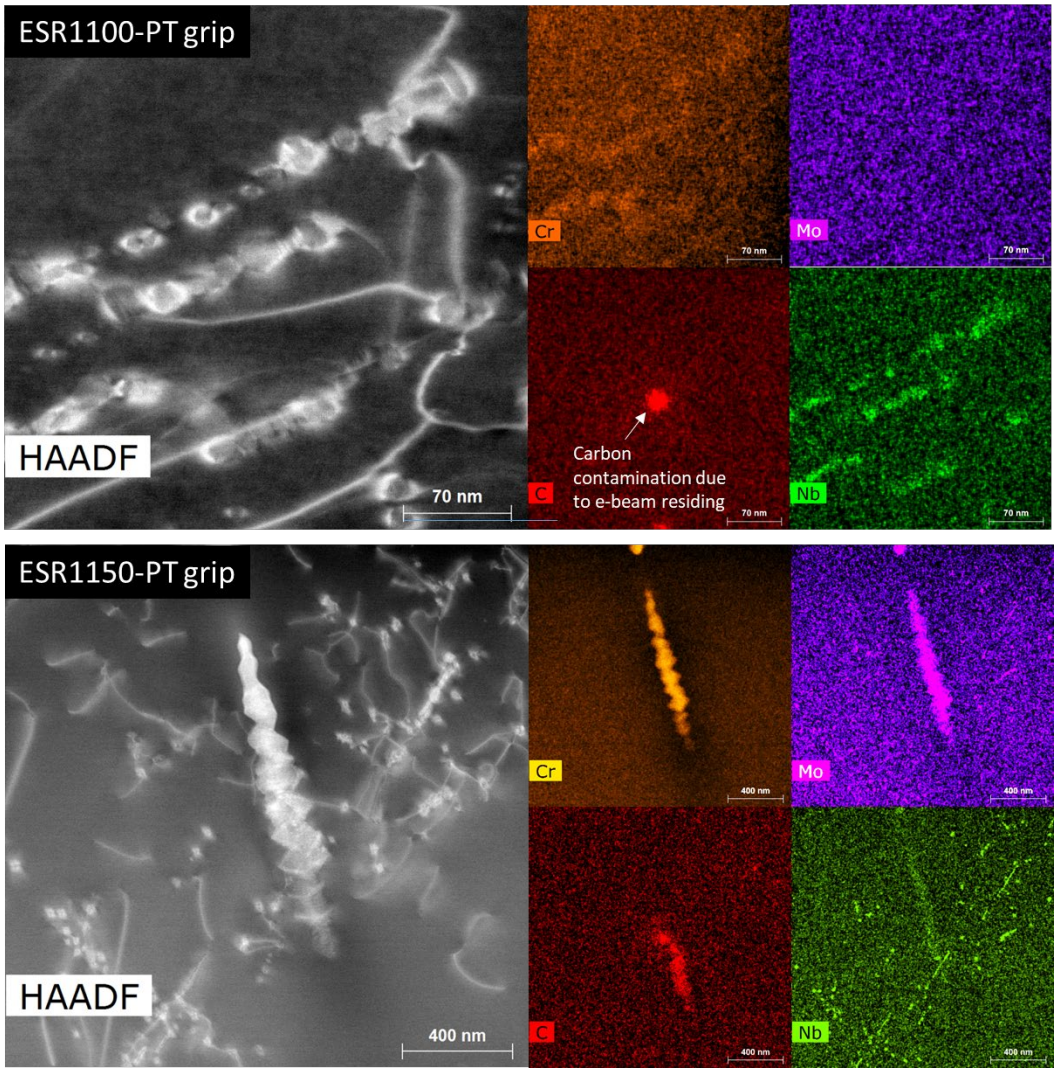

Figure 4-16. HAADF images and EDS elemental maps featuring the Z-phase precipitates on dislocations in the PT samples. The ESR1150-PT image also has one $M_{23}C_6$ chain included. Note the difference in the magnifications of the two samples.

5 Discussion

5.1 Effect of PT on creep life

The creep curves in Figure 2-1 and the creep data in Table 2-2 shows that the PT specimens under the 600°C/330MPa test condition have inferior creep resistance compared to the SA specimens. In order to explain the behavior, an understanding of the contribution to the creep strength from different microstructural features, including the solutes, the dislocations, and the secondary phase particles, is needed. The overall effect of those features results in an effective stress expressed as (Sandström et al., 2013):

$$\sigma_{eff} = \sigma_{appl} - \sigma_{disl} - \sigma_{PH} - \sigma_{sol} \ ,$$

where σ_{appl} is the applied stress, and σ_{disl}, σ_{PH} and σ_{sol} are strengthening contributions from dislocations, particles, and solutes, respectively. Of the five gauge samples studied in this report, the creep-deformed microstructures share many common features among them, two critical ones being the similarities in the dislocation cell sizes (Figure 4-3) and the 1-10 nm-sized MX precipitates on dislocations (Figure 4-10). It is widely accepted that the dislocation cell size is inversely proportional to the applied steady-state flow stress, which is also inversely proportional to the square root of the dislocation density (Orlová, 2001):

$$d \propto \sigma^{-1} \propto \rho^{-1/2} \ .$$

The fact that all the materials were loaded to the same stress level implies a similar dislocation cell size, which is in agreement with the experimental observation. Therefore, σ_{disl} from all the materials are of similar values. σ_{sol} is likely to be very trivial considering that the materials were tested at 600°C and extensive precipitation has occurred.

The major difference between the SA and the PT samples comes from σ_{PH}. σ_{PHi}, being the strengthening from particles of type *i*, is estimated based on the Orowan mechanism, which can be expressed as (He & Sandström, 2017; Sandström et al., 2013; Vujic et al., 2015):

$$\sigma_{PHi} = 0.8\frac{2\tau_L m}{bL_{\text{part}i}}$$

where b is the Burger's vector, τ_L is the dislocation line tension, $\tau_L = Gb^2/2$, m is the Taylor factor, and $L_{\text{part}i}$ is the average spacing between particles of a type *i* that is larger than a threshold size of r_{th} . If the particles are smaller than r_{th}, dislocations can climb over and no strengthening is provided. r_{th} can be expressed as (Sandström et al., 2013):

$$r_{th} = 2LM_{cl}b^2\sigma_{eff}\frac{\rho}{\dot{\varepsilon}m}$$

where M_{cl} is the dislocation climb mobility, L is the interparticle spacing, ρ is the dislocation density and $\dot{\varepsilon}$ is the creep rate. The specimens in the current study were tested at 600°C/330MPa, and it is the dislocation glide, rather than climb, being the dominate creep mechanism (Kestenbach,

Krause, & da Silveira, 1978). Therefore, r_{th} is expected to be very small and all the precipitates in the specimens contributes to the creep resistance.

It was found that all the gauge samples contains the 1-10 nm-sized Nb-rich precipitates on dislocations of similar density (Figure 4-10). Therefore, the σ_{PH} from those is expected to be close. One major difference in the precipitate structure is that the SA samples have a relatively high density of the co-existing $M_{23}C_6$ and $(Cr,Mo)_3Ni_2Si(C,N)$ η phases in the grain interior at ~ 0.5 μm spacing, while the PT samples is mostly free of those two phases except for some extended (μm-sized) precipitates of very low density (Figures 4-6 and 4-7). Therefore, the SA specimens have higher overall σ_{PH} compared to the PT specimens, resulting in smaller effective stresses, leading to longer creep rupture time.

As mentioned in the introduction section, the reduction of creep rupture life observed in the PT specimens diminished at higher temperatures and lower stresses, and at 925°C/27 MPa, limited data show that the ESR1150-SA and the ESR1150-PT have similar creep life (Rupp & McMurtrey, 2020a). This can possibly be explained as follows. In those high temperature, low stress conditions, the dislocation climb is becoming the dominant creep mechanism (Kestenbach et al., 1978). Also, higher temperatures lead to fewer, coarser precipitates in both SA and PT conditions. Therefore, the strengthening from precipitates losses its significance. However, detailed microstructural characterization will need to be performed to make a final conclusion.

5.2 Effect of PT on creep elongation

The creep curves in Figure 2-1 and the data in Table 2-2 show that the PT has significantly increased the total elongation at rupture, indicating that the creep cavity nucleation, growth or coalescence was hindered by the PT. Further investigation of the necking area using scanning electron microscopy will be performed to elucidate the mechanism.

6 Summary and Future Work

This work studied the deformation microstructures of five creep-tested specimens, namely AOD1100-SA, ESR1100-SA, ESR1150-SA, ESR1100-PT, and ESR1150-PT. The creep condition was 600°C/330MPa.

For the gauge samples, the microstructures between the SA and the PT samples shared two major similarities, one being the dislocation cell structure and the other being the nm-sized MX precipitates on dislocations. Meanwhile, there was one major difference being that the SA samples had a relatively high density of the co-existing $M_{23}C_6$ and $(Cr,Mo)_3Ni_2Si(C,N)$ η phases in the grain interior, while the PT samples was mostly free of those two phases except for some extended (μm-sized) precipitates of very low density. This difference led to the reduced precipitate strengthening in the PT specimens that could explain the observed shorter rupture life.

For the grip samples, the study showed that for the SA samples, the precipitates on dislocations, though relatively sparse, were 50-100nm sized $M_{23}C_6$. For the PT samples, the precipitates on dislocations were 20nm sized Z-phase, suggesting that they did not evolve much after 600°C for ~1000 hours from the as-received PT. Other types of precipitates are similar among all the specimens, except for that those that already existed from PT grew larger.

Future work involves the completion of the microstructural study of the fatigue and creep-fatigue deformed specimens to understand the significant increase in the cycles to failure from PT. Additional study of specimens from creep test conditions other than 600°C/330MPa, in particular at low temperature, low stress conditions and at high temperature, low stress conditions, may also be performed.

ACKNOWLEDGMENTS

The research was sponsored by the U.S. Department of Energy, under Contract No. DEAC02- 06CH11357 with Argonne National Laboratory, managed and operated by UChicago Argonne LLC, and under Contract No. DE-AC07-05ID14517 with Idaho National Laboratory, managed and operated by Battelle Energy Alliance. The electron microscopy study was performed at the Center for Nanoscale Materials, an Office of Science user facility, supported by the DOE, Office of Science, Office of Basic Energy Sciences, under Contract No. DE-AC02-06CH11357. Programmatic direction was provided by the Office of Nuclear Reactor Deployment of the Office of Nuclear Energy, U.S. Department of Energy.

The authors gratefully acknowledge the support provided by Sue Lesica, Federal Advanced Materials Lead, Advanced Reactor Technologies (ART) Program, Brian Robinson, Federal Manager, ART Fast Reactors (FR) Campaign, and Robert Hill of Argonne National Laboratory (ANL), National Technical Director, ART FR Campaign.

Helpful discussions with George Young of Kairos Power, Ryann Rupp, Michael McMurtrey and Richard Wright of Idaho National Laboratory, and Yanli Wang of Oak Ridge National Laboratory, are gratefully acknowledged.

REFERENCES

Ding, R., Yan, J., Li, H., Yu, S., Rabiei, A., & Bowen, P. (2019). Microstructural evolution of Alloy 709 during aging. *Materials Characterization, 154*, 400-423. doi:https://doi.org/10.1016/j.matchar.2019.06.018

He, J., & Sandström, R. (2017). Basic modelling of creep rupture in austenitic stainless steels. *Theoretical and Applied Fracture Mechanics, 89*, 139-146. doi:https://doi.org/10.1016/j.tafmec.2017.02.004

Kestenbach, H. J., Krause, W., & da Silveira, T. L. (1978). Creep of 316 stainless steel under high stresses. *Acta Metallurgica, 26*(5), 661-670. doi:https://doi.org/10.1016/0001-6160(78)90016-0

Li, M., Chen, W.-Y., Zhang, X., & Natesan, K. (2018). *Report on the Initial Loading of SS3 Specimens from the First Commercial Heat of Alloy 709 in Sodium Materials Test Loops for Long-term Exposure* (ANL-ART-135). Retrieved from https://www.osti.gov/servlets/purl/1485130

McMurtrey, M. (2018). *Report on the FY18 creep rupture and creep-fatigue tests on the first commercial heat of Alloy 709* (INL/EXT-18-46140-Rev000). Retrieved from https://www.osti.gov/servlets/purl/1484686

McMurtrey, M., & Rupp, R. E. (2019). *Report on FY-19 Scoping Creep and Creep-Fatigue Testing on Heat Treated Alloy 709 Base Metal* (INL/EXT-19-55502-Rev000). Retrieved from

Natesan, K., Zhang, X., & Li, M. (2018). *Report on the initiation of planned FY18 short and intermediate term creep rupture tests and creep-fatigue tests on the first commercial heat of Alloy 709* (ANL-ART-151). Retrieved from https://www.osti.gov/servlets/purl/1485134

Orlová, A. (2001). Subgrain size in view of the composite model of dislocation structure. *Materials Science and Engineering: A, 297*(1), 281-285. doi:https://doi.org/10.1016/S0921-5093(00)01697-X

Porter, T. D., Wang, Z., Gilbert, E. P., Kaufman, M. J., Wright, R. N., & Findley, K. O. (2021). Microstructure evolution of alloy 709 during static-aging and creep-fatigue testing. *Materials Science and Engineering: A, 801*, 140361. doi:https://doi.org/10.1016/j.msea.2020.140361

Rupp, R. E., & McMurtrey, M. D. (2020a). *Mechanical Properties of Aged A709* (INL/EXT-20-59630-Rev000). Retrieved from https://www.osti.gov/servlets/purl/1690144

Rupp, R. E., & McMurtrey, M. D. (2020b). *Status of INL Aged A709 Mechanical Testing* (INL/EXT-20-59501-Rev000). Retrieved from https://www.osti.gov/servlets/purl/1688795

Rupp, R. E., Wang, Y., Zhang, X., & Sham, T.-L. (2021). *Integrated FY-21 Elevated-Temperature Mechanical-Testing Results for Alloy 709 Code Case* (INL/EXT-21-64314-Rev000). Retrieved from

Sandström, R., Farooq, M., & Zurek, J. (2013). Basic creep models for 25Cr20NiNbN austenitic stainless steels. *Materials Research Innovations, 17*(5), 355-359. doi:10.1179/1433075X13Y.0000000120

Sham, S., & Natesan, K. (2017). *Code Qualification Plan for an Advanced Austenitic Stainless Steel, Alloy 709, for Sodium Fast Reactor Structural Applications*. Paper presented at the International Conference on Fast Reactors and Related Fuel Cycles: Next Generation

Nuclear Systems for Sustainable Development (FR17), Yekaterinburg, Russian Federation.

Sham, T.-L., Zhang, X., & Young, G. A. (2019). *Microstructural Characterization of Alloy 709 Plate Materials with Additional Heat Treatment Protocol* (ANL-ART-170). Retrieved from https://www.osti.gov/servlets/purl/1601459

Sourmail, T., & Bhadeshia, H. K. D. H. (2005). Microstructural evolution in two variants of NF709 at 1023 and 1073 K. *Metallurgical and Materials Transactions A, 36*(1), 23-34. doi:10.1007/s11661-005-0135-y

Vujic, S., Sandström, R., & Sommitsch, C. (2015). Precipitation evolution and creep strength modelling of 25Cr20NiNbN austenitic steel. *Materials at High Temperatures, 32*(6), 607-618. doi:10.1179/1878641315Y.0000000007

Zhang, X., Chen, W.-Y., & Caputo, A. (2021). In-situ ion irradiation study of alloy 709 stainless steels with different processing histories. *Journal of Nuclear Materials, 553*, 153052. doi:https://doi.org/10.1016/j.jnucmat.2021.153052

Zhang, X., & Sham, T.-L. (2020). *Report on the FY20 Characterization of Age Hardened Alloy 709 Materials* (ANL-ART-192). Retrieved from https://www.osti.gov/servlets/purl/1656885

Nuclear Science and Engineering Division

Argonne National Laboratory

9700 South Case Avenue

Argonne, IL 60439

www.anl.gov

Argonne National Laboratory is a U.S. Department of Energy laboratory managed by UChicago Argonne, LLC